Published in IET Electric Power Applications
Received on 19th April 2010
Revised on 27th July 2010
doi: 10.1049/iet-epa.2010.0108

ISSN 1751-8660

Improved sensorless control of a permanent magnet machine using fundamental pulse width modulation excitation

Y. Hua M. Sumner G. Asher Q. Gao K. Saleh

Department of Electrical and Electronic Engineering, University of Nottingham, Nottingham NG7 2RD, UK
E-mail: huayahan@hotmail.com

Abstract: A new method to estimate the rotor position of permanent magnet synchronous motor (PMSM) drives over a wide speed range, including zero frequency is introduced. The method measures the motor current derivative in response to the standard pulse width modulation (PWM) sequence to estimate rotor position. No additional signal injection or separate test vectors are required although modification is needed when narrow PWM voltage vectors occur. Three compensation techniques are proposed to improve the quality of the position estimation and reduce current distortion when narrow vectors are used for position estimation. Experimental results for sensorless speed and position control of a 4 kW PMSM verify the effectiveness of the proposed techniques.

1 Introduction

'Sensorless' control of AC motor drives has been developed over recent years to improve reliability and reduce cost of industrial variable speed drives. Shaft mounted position or speed sensors add to system cost as they require coupling to the motor and alignment, and this causes a high proportion of build and drive commissioning failures. Encoder signal wiring also reduces the reliability of commissioned drive systems. Sensorless control based on the fundamental electromechanical model performs badly in the low and zero speed range [1, 2] as the machine's back-EMF tends to zero as the rotor speed reduces and information is lost in noise and low measurement resolution. Therefore sensorless methods which track the inherent saliencies of a motor [3–9] have been developed. These saliencies can be caused by magnetic saturation or by the physical construction of the rotor. Most of these saliency tracking techniques fall into two categories. The first category injects continuous high frequency voltage or current into the machine [4–7]. The position information resides in the induced high frequency current or voltage signals. However, the position signal can be difficult to extract as it is corrupted by harmonics resulting from other secondary machine saliencies [5] and the non-linearity of the power converter [10, 11]. To increase the signal-to-noise ratio of the estimated position measurements, the carrier amplitude must be increased and this leads to significant torque ripple and acoustic noise within the drive system. Signal injection techniques can only be implemented at very low speeds, unless combined with a model-based approach [12, 13].

The second category exploits the transient current responses to pulse width modulation (PWM) switching states. The INFORM method [4] uses transient excitation to acquire the rotor position, by using test vectors applied during the null vector of a PWM period. The use of separate test vectors results in extra losses, increased common mode current and voltage stress in the motor, and therefore the integration of test vectors into the standard PWM waveform is preferred, as proposed in [8, 9], however, both schemes still require special test vectors at very low operating speeds.

A more attractive approach is to use the normal fundamental PWM sequence as the 'test vector' [14, 15] – termed here the 'fundamental PWM excitation' (FPE) method. The current derivatives for two active vectors and the null vectors are measured over successive normal PWM switching cycles. No special test vectors are required and additionally FPE can be employed over a wide speed range. However, the main difficulty of integrating the position estimation scheme within the fundamental PWM sequence arises from the parasitic effects within the drive system. Parasitic effects such as inter-turn capacitance in the motor, capacitance of the insulation between the insulated gate bipolar transistor (IGBT) and the heatsink, and so on result in high frequency current oscillations when the IGBTs switch states, and these take a few microseconds to die down. The current derivatives required for the position estimation cannot be measured until these oscillations have disappeared. When the current derivative response to a particular switching vector must be measured, that vector must have a minimum duration t_{min}. Vectors shorter than t_{min} must be extended if position estimation is required during that switching period, and this results in significant distortion of the motor current [14, 15].

This paper introduces three techniques to improve the sensorless drive operation when using FPE. A pulse extension/compensation scheme is proposed which reduces

the distortion introduced into the motor line current when a narrow vector has to be extended. A simple compensation algorithm is proposed to eliminate common mode high frequency oscillations from the current derivative measurements. Finally, differential mode high frequency oscillations are reduced substantially by modifying the IGBT drive circuit, to slow down the IGBT switching only when a narrow vector is detected. Experimental results are presented to demonstrate the effective sensorless control of a surface mounted permanent magnet synchronous machine (PMSM) using the proposed techniques.

2 Position estimation using fundamental PWM sequence

The stator inductances of a three-phase, star-connected surface mounted PMSM are modulated by main flux saturation and therefore can be modelled by (1) [3]

$$\begin{aligned} l_{\sigma a} &= l_0 + \Delta l \cos(2\theta_e) \\ l_{\sigma b} &= l_0 + \Delta l \cos(2(\theta_e - 2\pi/3)) \\ l_{\sigma c} &= l_0 + \Delta l \cos(2(\theta_e - 4\pi/3)) \end{aligned} \tag{1}$$

where l_0 is the average stator inductance and Δl is the inductance variation due to modulation by the main flux. Thus, the main flux position θ_e can be tracked by monitoring the inductance variation. This process is now described.

When a PWM waveform is applied to a PM machine, the stator phase current response is described by (2)

$$\boldsymbol{u}_s = r_s \boldsymbol{i}_s + l_\sigma \frac{\mathrm{d}i_s}{\mathrm{d}t} + \boldsymbol{e} \tag{2}$$

where $\boldsymbol{u}_s$ and $\boldsymbol{i}_s$ are the stator voltage and current vectors, $\boldsymbol{r}_s$ and l_σ are the stator resistance and inductance, and $\boldsymbol{e}$ is the back-emf vector. The PWM scheme uses the six active and two null switching states of a three-phase inverter, defined as $V_1(1,\ 0,\ 0)$, $V_2(1,\ 1,\ 0)$, $V_3(0,\ 1,\ 0)$, $V_4(0,\ 1,\ 1)$, $V_5(0,\ 0,\ 1)$, $V_6(1,\ 0,\ 1)$ and $V_0(0,\ 0,\ 0)$, $V_7(1,\ 1,\ 1)$ in the format $V_x(a,\ b,\ c)$, where V_x is the vector name and $(a,\ b,\ c)$ gives the switch state of each inverter leg. The phase current transient responses to the excitation of these voltage vectors can be derived from (2). In a star-connected PMSM, taking $V_1(1,0,0)$ as the applied voltage vector, the three stator voltages are

$$\begin{aligned} U_{\mathrm{DC}} &= i_a^{(1)} r_s + l_{\sigma a} \frac{\mathrm{d}i_a^{(1)}}{\mathrm{d}t} + e_a^{(1)} - i_b^{(1)} r_s - l_{\sigma b} \frac{\mathrm{d}i_b^{(1)}}{\mathrm{d}t} - e_b^{(1)} \\ 0 &= i_b^{(1)} r_s + l_{\sigma b} \frac{\mathrm{d}i_b^{(1)}}{\mathrm{d}t} + e_b^{(1)} - i_c^{(1)} r_s - l_{\sigma c} \frac{\mathrm{d}i_c^{(1)}}{\mathrm{d}t} - e_c^{(1)} \\ -U_{\mathrm{DC}} &= i_c^{(1)} r_s + l_{\sigma c} \frac{\mathrm{d}i_c^{(1)}}{\mathrm{d}t} + e_c^{(1)} - i_a^{(1)} r_s - l_{\sigma a} \frac{\mathrm{d}i_a^{(1)}}{\mathrm{d}t} - e_a^{(1)} \end{aligned} \tag{3}$$

where U_{DC} is the DC-link voltage, and the superscript (1) denotes quantities measured in response to voltage vector V_1. A similar set of equations derived from applying the closest null vector in the PWM sequence, V_0 is given in (4).

$$\begin{aligned} 0 &= i_a^{(0)} r_s + l_{\sigma a} \frac{\mathrm{d}i_a^{(0)}}{\mathrm{d}t} + e_a^{(0)} - i_b^{(0)} r_s - l_{\sigma b} \frac{\mathrm{d}i_b^{(0)}}{\mathrm{d}t} - e_b^{(0)} \\ 0 &= i_b^{(0)} r_s + l_{\sigma b} \frac{\mathrm{d}i_b^{(0)}}{\mathrm{d}t} + e_b^{(0)} - i_c^{(0)} r_s - l_{\sigma c} \frac{\mathrm{d}i_c^{(0)}}{\mathrm{d}t} - e_c^{(0)} \\ 0 &= i_c^{(0)} r_s + l_{\sigma c} \frac{\mathrm{d}i_c^{(0)}}{\mathrm{d}t} + e_c^{(0)} - i_a^{(0)} r_s - l_{\sigma a} \frac{\mathrm{d}i_a^{(0)}}{\mathrm{d}t} - e_a^{(0)} \end{aligned} \tag{4}$$

As the sampling instants for V_1 and V_0 are very close to each other (less than one PWM period), the back-emf and stator resistance voltage drop can be assumed to be approximately the same in (3) and (4) and can be eliminated. Combining (3) and (4) yields

$$\begin{aligned} U_{DC} &= \left(l_{\sigma a} \frac{\mathrm{d}i_a^{(1)}}{\mathrm{d}t} - l_{\sigma a} \frac{\mathrm{d}i_a^{(0)}}{\mathrm{d}t} \right) - \left(l_{\sigma b} \frac{\mathrm{d}i_b^{(1)}}{\mathrm{d}t} - l_{\sigma b} \frac{\mathrm{d}i_b^{(0)}}{\mathrm{d}t} \right) \\ 0 &= \left(l_{\sigma b} \frac{\mathrm{d}i_b^{(1)}}{\mathrm{d}t} - l_{\sigma b} \frac{\mathrm{d}i_b^{(0)}}{\mathrm{d}t} \right) - \left(l_{\sigma c} \frac{\mathrm{d}i_c^{(1)}}{\mathrm{d}t} - l_{\sigma c} \frac{\mathrm{d}i_c^{(0)}}{\mathrm{d}t} \right) \\ -U_{DC} &= \left(l_{\sigma c} \frac{\mathrm{d}i_c^{(1)}}{\mathrm{d}t} - l_{\sigma c} \frac{\mathrm{d}i_c^{(0)}}{\mathrm{d}t} \right) - \left(l_{\sigma a} \frac{\mathrm{d}i_a^{(1)}}{\mathrm{d}t} - l_{\sigma a} \frac{\mathrm{d}i_a^{(0)}}{\mathrm{d}t} \right) \end{aligned} \tag{5}$$

Incorporating (1) into (5) and rearranging yields

$$\begin{aligned} \frac{\mathrm{d}i_a^{(1)}}{\mathrm{d}t} - \frac{\mathrm{d}i_a^{(0)}}{\mathrm{d}t} &= \frac{\mathrm{d}i_a^{(10)}}{\mathrm{d}t} = \frac{1}{g}\left(2 - \frac{\Delta l}{l_0}\cos(2\theta_e)\right) \\ \frac{\mathrm{d}i_b^{(1)}}{\mathrm{d}t} - \frac{\mathrm{d}i_b^{(0)}}{\mathrm{d}t} &= \frac{\mathrm{d}i_b^{(10)}}{\mathrm{d}t} = -\frac{1}{g}\left(1 + \frac{\Delta l}{l_0}\cos\left(2\left(\theta_e - \frac{4\pi}{3}\right)\right)\right) \\ \frac{\mathrm{d}i_c^{(1)}}{\mathrm{d}t} - \frac{\mathrm{d}i_c^{(0)}}{\mathrm{d}t} &= \frac{\mathrm{d}i_c^{(10)}}{\mathrm{d}t} = -\frac{1}{g}\left(1 + \frac{\Delta l}{l_0}\cos\left(2\left(\theta_e - \frac{2\pi}{3}\right)\right)\right) \end{aligned} \tag{6}$$

where $g = 3l_0(1 - (\Delta l/2l_0)^2)/U_{\mathrm{DC}}$. The superscript (10) denotes the combination of quantities measured during V_1 and V_0.

The flux position vector $\boldsymbol{p}_s$ can be defined as [3]

$$\begin{aligned} \boldsymbol{p}_s &= \frac{\Delta l}{l_0}(p_a + \alpha p_b + \alpha^2 p_c) = \frac{\Delta l}{l_0}\Bigg(\cos(2\theta_e) \\ &\quad + \alpha\cos\left(2\left(\theta_e - \frac{2\pi}{3}\right)\right) + \alpha^2\cos\left(2\left(\theta - \frac{4\pi}{3}\right)\right)\Bigg) \end{aligned} \tag{7}$$

where $\alpha = e^{j(2\pi/3)}$.

The position vector defined in (7) can now be expressed in terms of the measured current transients of (6) as

$$\begin{aligned} p_a &= 2 - g\frac{\mathrm{d}i_a^{(10)}}{\mathrm{d}t}, \quad p_b = -1 - g\frac{\mathrm{d}i_c^{(10)}}{\mathrm{d}t}, \\ p_c &= -1 - g\frac{\mathrm{d}i_b^{(10)}}{\mathrm{d}t} \end{aligned} \tag{8}$$

The position angle cannot be derived from (8) alone. Excitation from another active voltage vector is required. In sector I, the other active vector is V_2. Similar position

doi: 10.1049/iet-epa.2010.0108

signals can be calculated during V_2 and V_7 as given in (9).

$$p_a = -1 + g\frac{\mathrm{d}i_a^{(27)}}{\mathrm{d}t}, \quad p_b = -1 + g\frac{\mathrm{d}i_c^{(27)}}{\mathrm{d}t}, \quad p_c = 2 + g\frac{\mathrm{d}i_b^{(27)}}{\mathrm{d}t} \tag{9}$$

where the superscript (27) denotes the combination of quantities measured during V_2 and V_7. The position vector can be constructed by selecting the position scalars with the cancellable offsets from (8) and (9). Such as

$$\boldsymbol{p} = p_a + \alpha p_b + \alpha^2 p_c = \left(-1 + g\frac{\mathrm{d}i_c^{(27)}}{\mathrm{d}t}\right) + \alpha\left(-1 - g\frac{\mathrm{d}_c^{(10)}}{\mathrm{d}t}\right) + \alpha^2\left(-1 - g\frac{\mathrm{d}_b^{(10)}}{\mathrm{d}t}\right) \tag{10}$$

where the offset '-1' in the position scalar equations can then be eliminated. A unique estimate of the rotor position can be achieved using only measurement of current derivatives in response to specific applied voltage vectors. Other combinations of measured current derivative in response to specific voltage vectors can be derived for the other PWM sectors, as described in [14, 15].

3 Current switching oscillations

The main difficulty when applying current derivative-based position estimation schemes to real systems arises from the parasitic effects within the motor, the inverter and the cabling. The high dv/dt caused by power device switching excites parasitic capacitances distributed in the system, and causes high frequency current oscillations. Based on high frequency system modelling and the analysis of the electromagnetic interference effects, the switching oscillations can be categorised as common mode and differential mode components [16]. The common mode oscillation is caused by the currents flowing between the inverter phase circuits and the system ground, for example, through capacitance between the IGBT and the grounded heatsink, or capacitance between a motor winding and the stator iron itself due to the winding insulation. When one phase is switched ON/OFF, the differential mode oscillation on the inverter output results from similar parasitic paths (i.e. stray capacitance) between the switched phase and the other two phases.

To illustrate the behaviour of the experimental system used in this project, the output current of one inverter phase together with the IGBT heatsink earth current and the AC power supply earth current are shown in Fig. 1 for one switching instant. Two frequency ranges are found in the common mode oscillation. The lower range (100–200 kHz) is the current which penetrates into the stator windings and flows through the supply inductors. This component exists in the earth conductor of both the supply cable and the machine cable. The other component is the small high frequency oscillation (above 2 MHz) which appears only at the grounding point on the inverter's output side. The common mode current at this frequency is blocked by the impedance of the supply inductance and the machine's stator windings. The differential mode current flows between three phases and so only appears in the output current. It has a high amplitude and a frequency around 2–3 MHz. If the motor current, or current derivative are to be measured for position estimation, it can be seen from Fig. 1 that the measurement must be delayed by 8 μs ($t_{\min}$) from the switching edge, so that these oscillations do not corrupt the measurement. However, $t_{\min}$ should be kept as small as possible in order to minimise the incurred distortion in the motor current.

4 Switching vector extension and compensation

Narrow voltage vectors must be extended to a minimum vector duration $t_{\min}$, which is set according to the high frequency oscillation decay time. Because the voltage time area in each PWM period should not be changed, any vector extension must be compensated. Fig. 2 shows a simple extension and compensation scheme applied when the stator voltage vector is in sector I [14, 15]. Both switching edges of phase a are shifted to make V_1 wide enough during the first half PWM period, and the ON time

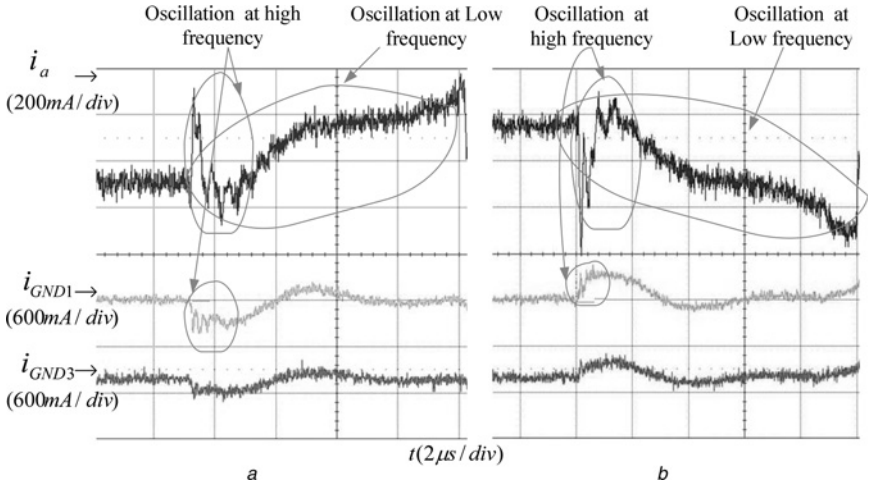

Fig. 1 *Current waveforms*

a Device turn-on
b Device turn-off
Top – the output current i_a; middle – the heatsink ground current at the inverter output point iGND1; bottom – the ground current at the power supply point iGND2

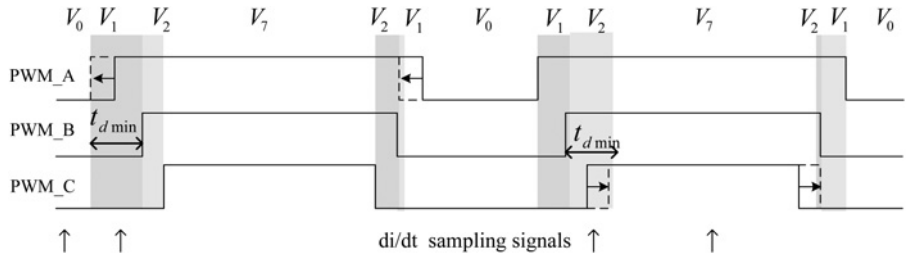

Fig. 2 *PWM sequence in sector I with active vectors being extended to t_{min}*

on each phase is kept unchanged. The current derivative signals can then be measured during V_1 and V_0. If it does not meet the minimum duration $t_{\min}$, the other active vector, V_2, is extended and compensated by moving the switching edges of phase c in the second PWM period. The position vector is then obtained from the di/dt signals measured during V_1, V_2, V_0 and V_7, as described in Section 2. Modifying the standard PWM sequence when necessary [14, 15] can cause additional motor current distortion, and this results in torque ripple and acoustic noise. These effects should therefore be minimised.

A new method is introduced here to study the current ripple during one PWM period. In a space vector PWM voltage source inverter (VSI), the stator voltage reference vector is implemented using a voltage vector switching sequence. The magnitude of these switching state vectors is normalised with respect to the DC-link voltage. For example, the reference voltage vector $\boldsymbol{u}_s^*$ with magnitude of $U_{DC}/2$ and phase angle α in sector I is shown in Fig. 3. The durations of the active vectors V_1 and V_2, that is, t_1 and t_2, are represented by the lengths of the vectors on the vector plot. In each PWM period, the null vector time for V_0 and V_7, are set to half the total null vector time.

There will be an error between the instantaneous voltage vector and the reference vector. The voltage errors corresponding to the active vectors V_1, V_2 and zero vectors V_0 (V_7) can be expressed as

$$\begin{aligned}\Delta V_{1-\text{ref}} &= V_1 - \boldsymbol{u}_s^* \\ \Delta V_{2-\text{ref}} &= V_2 - \boldsymbol{u}_s^* \\ \Delta V_{0-\text{ref}} &= \Delta V_{7-\text{ref}} = -\boldsymbol{u}_s^*\end{aligned} \tag{11}$$

These voltage errors that are referred to the reference vector can be defined as the 'voltage ripple vector', represented by $\boldsymbol{u}_{\text{ripple}}$, and the time integrals of these error voltage vectors determine the distortion in the output voltage [17] and the stator current. A measure of the phase current ripple can be defined correspondingly as 'current ripple vector', $\boldsymbol{i}_{\text{ripple}}$. If the stator resistance voltage and the back-emf are neglected, the voltage and current ripple vectors are orthogonal. That is, at very low speed, $u_d \simeq L_d$ (di_d/dt), $u_q \simeq L_q$ (di_q/dt), where L_d and L_q are the orthogonal total inductance on the rotating reference frame. Also, in a PMSM, the ripple vectors can be resolved along the d and q axes, in the reference frame synchronous with the rotating reference vector $\boldsymbol{u}_s^*$. The q-axis, in accordance with the torque current direction, is aligned with $\boldsymbol{u}_s^*$.

Fig. 4*a* illustrates the voltage ripple vector plot for one fundamental PWM cycle. The switching sequence in the first half cycle is indicated by the black line and that in the second half cycle is indicated by the grey line. Accordingly, in Fig. 4*b* the d and q-axis voltage and current ripple are plotted against time. The total current harmonic distortion can be evaluated by summing the areas confined by the ripple waveforms and the zero axes. The magnitudes of both voltage ripple and current ripple over one fundamental PWM period therefore depend on the reference vector and the employed switching sequence.

4.1 Simple vector compensation scheme

The current ripple caused by the PWM vector extension and compensation schemes used in the saliency position estimation based on the FPE can now be studied. When the

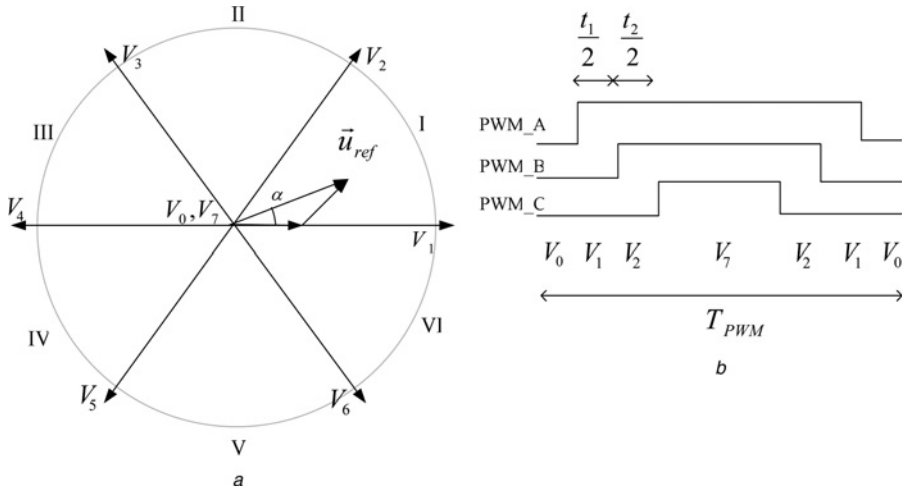

Fig. 3 *Standard fundamental PWM*

a Vector plot
b Switching sequence

doi: 10.1049/iet-epa.2010.0108

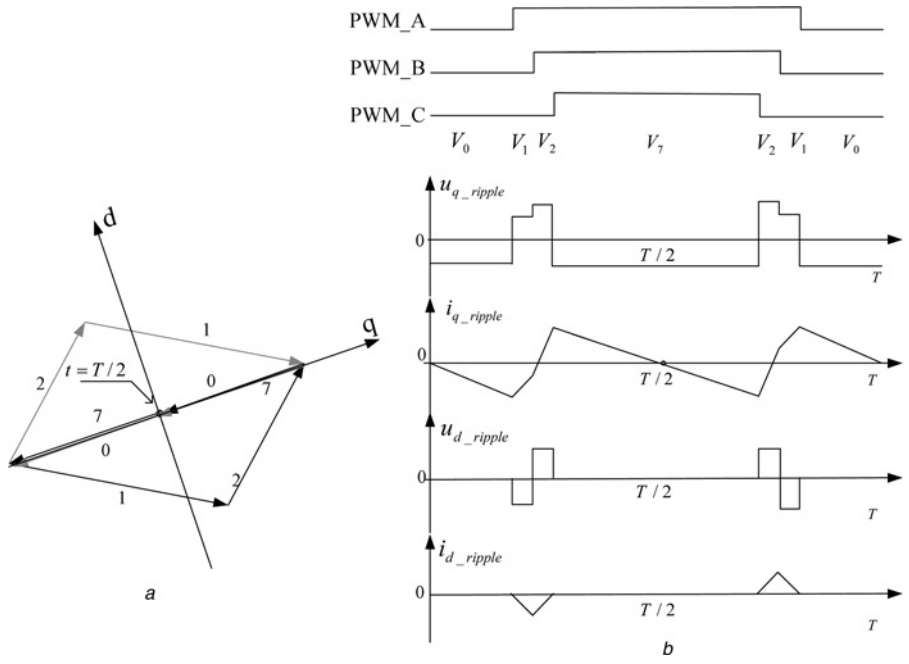

Fig. 4 *Voltage and current ripple of the standard fundamental PWM sequence*

a Vector plot of voltage ripple
b Voltage and current ripples in the $d-q$ reference frame

reference voltage vector is in sector I and V_1 needs to be extended for correct d*i*/d*t* sampling, the resultant voltage and current ripple vectors are plotted in Fig. 5. The dashed line indicates the ripple vector of the standard fundamental PWM sequence (without extension) for comparison. As can be seen, the main disadvantage of this scheme is that a large current deviation from the fundamental current ripple exists during the long inactive period of V_7, although this offset is compensated later. Significant deviations exist in both the d and q-axis current components.

4.2 Improved vector compensation scheme

To reduce this additional current deviation, a modified compensation scheme is proposed where the compensation is made in advance. When an active voltage vector needs

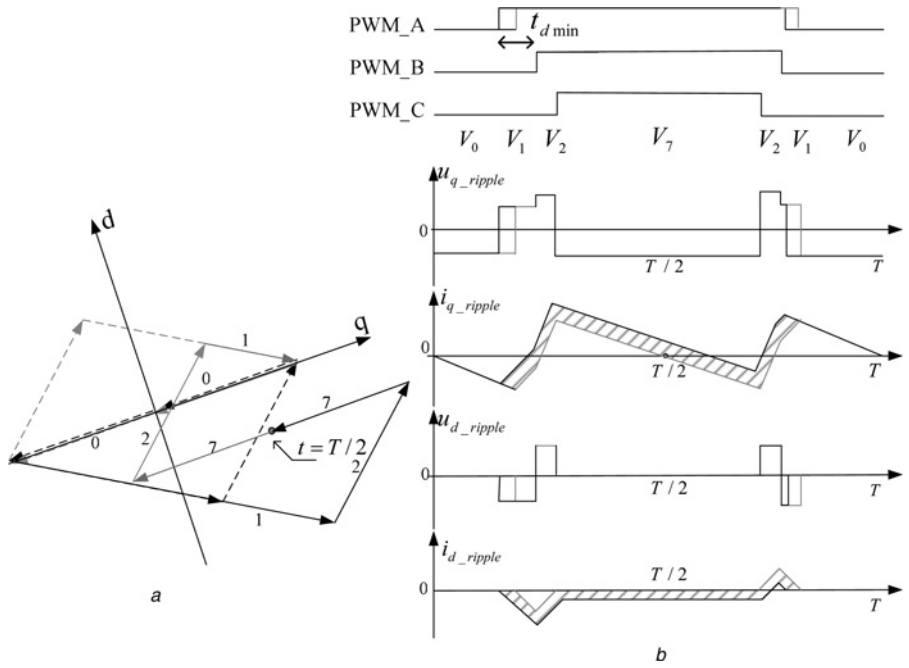

Fig. 5 *Voltage and current ripples of the PWM with extension of V_1*

a Vector plot of voltage ripple
b Voltage and current ripples in the $d-q$ reference frame

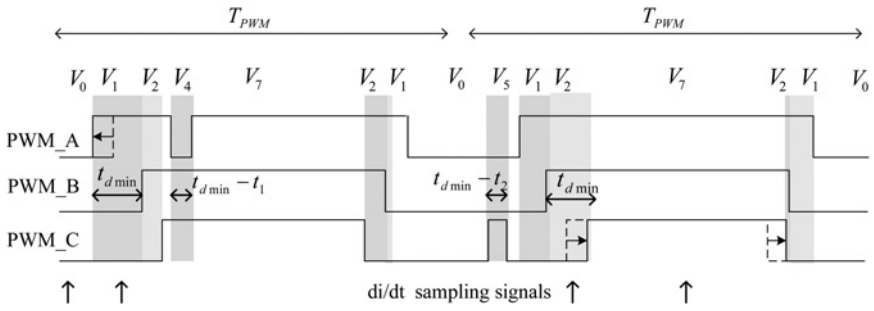

Fig. 6 *PWM sequence with extension of V_1 and V_2 in sector I using improved compensation scheme*

to be extended by a time t_{ext} to t_{min}, its opposite voltage vector should be applied during the close null vector, with a width equal to the extension t_{ext}. Fig. 6 shows operation for sector I. $V_1(t_1)$ is not long enough and is therefore extended to t_{min}. The opposite vector V_4 is then inserted at the beginning of V_7 to compensate this effect, with a duration equal to the extended part t_{ext} ($t_{ext} = t_{min} - t_1$). In the second PWM period, if V_2 is extended, its opposite vector V_5 is added for compensation. The current ripple introduced by this method is plotted in Fig. 7. By comparing Fig. 7 with Fig. 5, it can be seen that the current deviation is much lower, that is, the current deviation is reduced by this improved compensation scheme. This compensation still avoids the switching of two phases at the same instant and therefore no additional voltage stress is put on the winding insulation.

To illustrate the current distortion quantitatively, the stator currents measured on the experimental system described in Section 6 are presented for these two extension/compensation schemes. The PM machine is controlled at 100 rpm without an external load. The PWM period is 100 μs and t_{min} is set as 8 μs (note that no common mode or differential mode compensation has been incorporated as yet). Fig. 8*a* shows the phase current and the PWM sequence when $\boldsymbol{u}_s^*$ is located in the middle of sector I and the simple compensation scheme is used. The large current deviation due to the pulse extension can be observed in the middle of the waveform.

The current waveform for operation with the improved compensation scheme is shown in Fig. 8*b*. There is a significant reduction in the current deviation when compared to the simple compensation scheme. Bringing forward the compensation can effectively reduce the distortion caused by the vector compensation.

5 Reduction of common mode and differential mode effects

The vector extension and compensation schemes bring about additional current ripple. For this reason, if the effect of the current switching oscillations can be reduced, the vector extension can be minimised, and thus the current ripple can be suppressed.

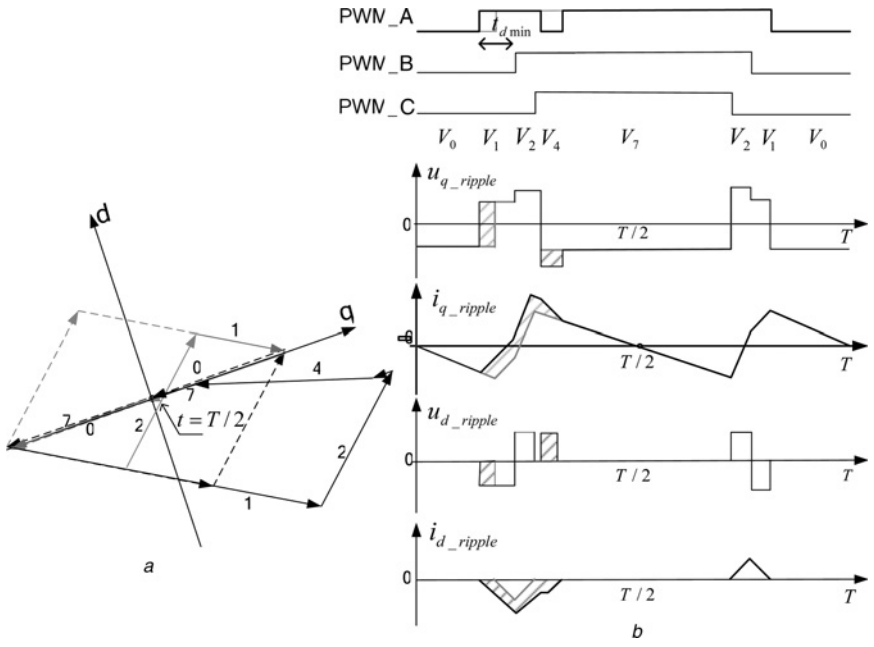

Fig. 7 *Voltage and current ripples of the PWM with extension of V_1 and improved compensation*

a Vector plot of voltage ripple
b Voltage and current ripples in the *d*–*q* reference frame

doi: 10.1049/iet-epa.2010.0108

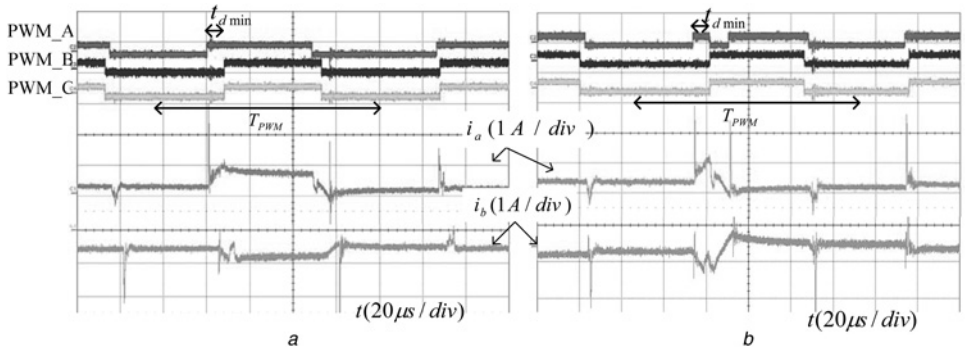

Fig. 8 *Current ripple for different compensation schemes*

a Simple compensation scheme
b Improved compensation scheme

5.1 Reduction of measured common mode noise

Normally for the AC inverter, if the three-phase layout is balanced and cables are the same, the common mode currents ($i_{com\,a}$, $i_{com\,b}$, $i_{com\,c}$) flow equally through three phases, and the ground current is the sum of them. The motor currents are

$$\begin{aligned} i_a &= i_{a1} + i_{com\,a} \\ i_b &= i_{b1} + i_{com\,b} \\ i_c &= i_{c1} + i_{com\,c} \end{aligned} \tag{12}$$

where i_{a1}, i_{b1}, i_{c1} are the current components without common mode noise and

$$i_{a1} + i_{b1} + i_{c1} = 0 \tag{13}$$

Therefore

$$i_{com\,a} = i_{com\,b} = i_{com\,c} = \frac{1}{3}(i_a + i_b + i_c) \tag{14}$$

A similar relationship exists for the current derivatives, that is

$$\frac{di_{com\,a}}{dt} = \frac{di_{com\,b}}{dt} = \frac{di_{com\,c}}{dt} = \frac{1}{3}\left(\frac{di_a}{dt} + \frac{di_b}{dt} + \frac{di_c}{dt}\right) \tag{15}$$

Using these equations, the common mode noise can be removed from the measured di/dt signals by subtracting (15) from each di/dt measurement. The effect of the common mode compensation on the estimated position signals in the experimental system is shown in Fig. 9. It is clear that the common mode components appearing in the position signals are significantly reduced.

5.2 Reduction of differential mode noise – changeable IGBT gate resistance

To reduce both common mode and differential mode current oscillations, when di/dt measurements need to be made for position estimation, it is possible to change the rate of change of inverter output voltage. One method is to add a snubber circuit, which can reduce dv/dt by transferring the high frequency switching energy from the IGBT output to an energy storage element. For this work snubber capacitors have been added and the output voltage spikes are eliminated, but the duration of current switching oscillations are not significantly reduced.

The new method proposed here is to increase the IGBT gate resistance. The gate resistance has a significant impact on the dynamic performance of the IGBT switching. A smaller gate resistance will charge and discharge the gate capacitance faster, reducing the switching time and switching losses, while causing a high dv/dt. A larger gate resistance will reduce dv/dt at the output (and the associated high frequency oscillations) at the expense of additional switching losses. A gate drive circuit providing a changeable gate resistance has been developed and applied as shown in Fig. 10. R_{G1} and R_{G2} are connected in parallel. The bi-directional switch, which is realised by a MOSFET circuit, is controlled as part of the main control algorithm. During normal operation, this switch is turned ON and the nominal gate resistance for normal operation of the inverter (the parallel value of R_{G1} and R_{G2}) is connected in the circuit. When stator di/dt signals are to be measured for position estimation, the gate resistance is increased by turning OFF the MOSFET switch.

The turn-on waveforms of the gate driving voltage v_{GE}, the output voltage v_{CE} and the output current i_o of the lower

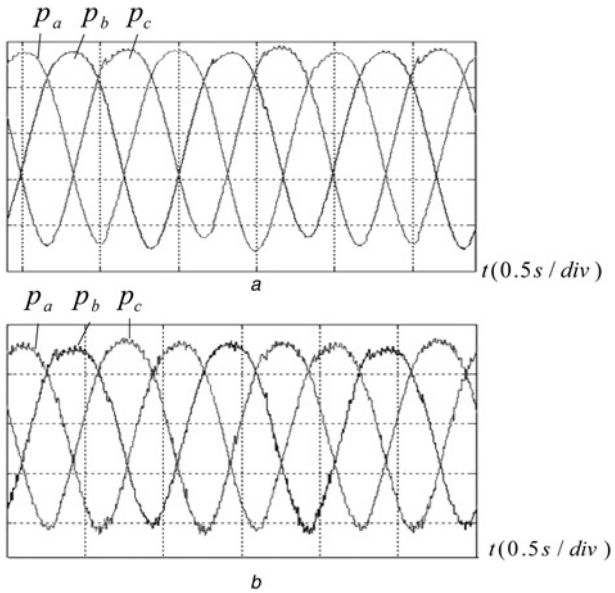

Fig. 9 *Estimated position signals*

a Without cancellation of the common mode noise
b With cancellation of the common mode noise

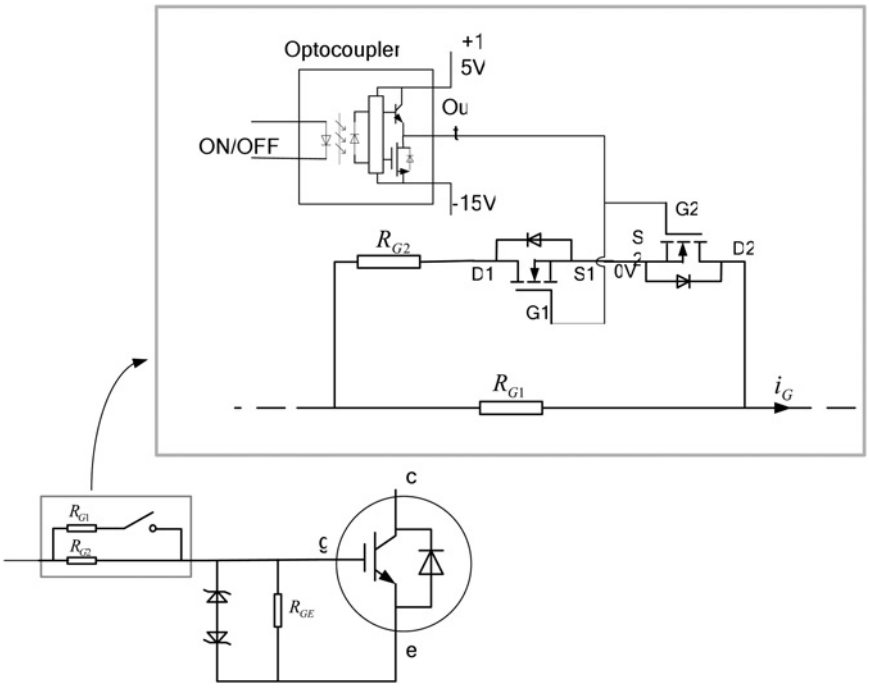

Fig. 10 *IGBT gate drive with changeable gate resistance*

IGBTs in one phase bridge, during one switching instant, are shown in Fig. 11. The IGBT type is SKM 50 GB 123D [18]. The recommended gate resistance is $R_G = 28\ \Omega$. A value of $R_G = 56\ \Omega$ has been chosen for use when taking di/dt measurements. This value was selected as it extends the turn-on time from 420 to 700 ns, and also extends the turn-off time from 80 to 120 ns [18]. From consultation with [18], the increase in switching loss per switching operation is acceptable, and it should be noted that this increased loss only occurs when a narrow switching vector is demanded from the PWM unit and a current derivative measurement is required.

The current waveforms in Fig. 11 can be compared directly. The high frequency oscillations, both on the current i_o and on the voltage v_{CE}, are much reduced with the larger gate resistance. When $R_G = 28\ \Omega$, v_{CE} falls from 620 to 0 V within less than 0.5 μs and the current oscillation lasts about 5 μs. When $R_G = 56\ \Omega$, v_{CE} settles at its steady state in about 1 μs. The current settling time is just less than 3 μs. With reduced current switching oscillations, the minimum vector width t_{min} can be decreased to 5 μs and by using this value the motor current ripple can be reduced.

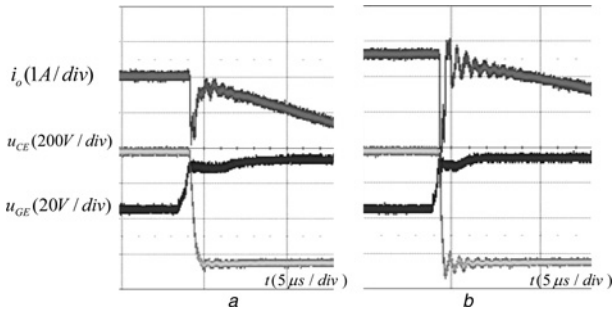

Fig. 11 *IGBT turn-on waveforms*
a $R_G = 56\ \Omega$
b $R_G = 28\ \Omega$

For the system developed, the FPE method was implemented every fourth PWM cycle. The test rig was operated using a minimum pulse width of 5 μs only when the FPE method is implemented. It was found that when operating at 1 Hz (electrical), a minimum pulse width was required for every PWM vector when the FPE method was implemented, that is, for 25% of the total number of switching pulses per fundamental period. That means that the larger gate resistance (and the improved vector compensation scheme with its additional power switch commutation) was used for 25% of the total number of switching pulses per fundamental period: this is an indication of the increase in switching losses associated with the proposed improvements for the sensorless control algorithm. For operation at 1 Hz and full load, this reduces to 24.8%. Similarly for operation at 15 Hz, no load, the increased gate resistance is used 21% of the time, reducing to 14% at full load. For operation at 50 Hz (1/3 rated speed), the increased gate resistance is used 8% of the time on no load and full load. This will only be of significance if the drive is to be operated at low or zero speed for sustained periods of time, in which case, additional cooling may be required.

6 Experimental setup and results

A 20 kW power converter was constructed for this research and used to drive a commercial surface mounted PMSM (4 kW, 6 pole, 3000 rpm). The overall structure of both the power converter and the control system is shown in Fig. 12. The control system is realised through a DSP-FPGA coordinated control platform.

The speed and position signals used for sensorless control are obtained using the position estimation scheme based on FPE. The raw position signal contains harmonics, predominately at $4f_e$ and $8f_e$ which are present in the machine due to higher order geometrical and saturation saliencies [5, 19]. An adaptive disturbance identifier is employed to eliminate these harmonics. A mechanical

doi: 10.1049/iet-epa.2010.0108

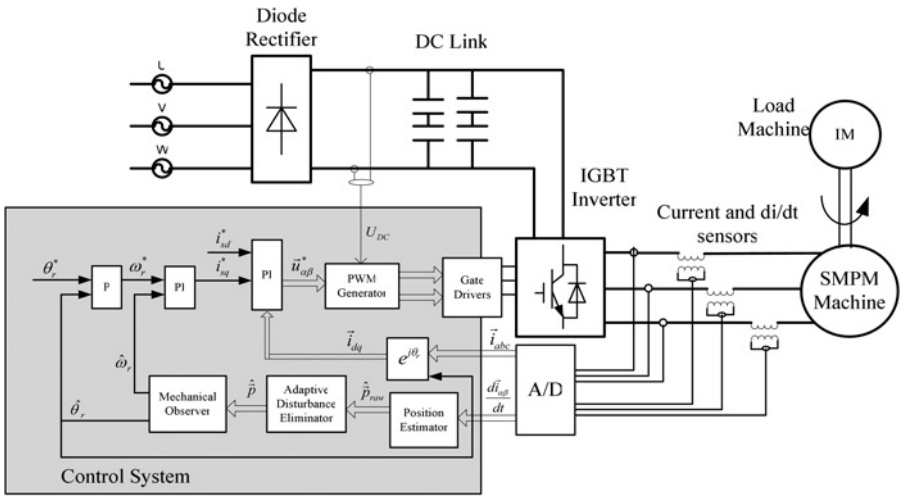

Fig. 12 *Overall structure of the sensorless control system*

observer is also used to improve the dynamic response of the estimated position and speed signals [14]. A final compensation is introduced to compensate the 'armature reaction effect', whereby the identified angle follows the main saturation saliency rather than the magnet position. This compensation angle is derived as a function of load from a pre-commissioned lookup table [15].

The transient current responses are measured through specially designed d*i*/d*t* sensors. Three bespoke air-core mutual inductors are used [3, 14]. The sensor has two layers of closely coupled windings. The stator current passes through the primary winding and the induced voltage across the secondary winding which is proportional to the stator current derivative is measured (As part of on-going work, the d*i*/d*t* will in future be obtained from the current sensor measurement.).

To quantify the improvement to the motor current waveform due to the effects described in this paper, the measured total harmonic distortion (THD) of the stator current is analysed. To demonstrate the change due to the improved vector compensation scheme of Section 4, Table 1 shows the THD of the stator current for different control schemes operating at 2 Hz and full load. The schemes employed are sensored vector control (i.e. the benchmark where $t_{\min} = 0$), sensorless control using the improved INFORM method reported in [20] and the FPE method proposed in this paper with the two vector compensation schemes described in Section 4. The minimum vector width $t_{\min}$ used for these results was set to 5 μs, and the common mode correction was also employed. The FPE method with improved compensation scheme clearly has a lower THD compared to the other sensorless methods.

To quantify explicitly the improvement due to the use of variable gate resistance for differential mode reduction, the system was operated with the improved compensation and the common mode cancellation. By reducing the minimum vector time duration or the test vector width $t_{d\min}$ from 8 to 5 μs (by using the modified gate drive circuit), the THD of the motor current at 2 Hz and full load reduces from 11.68 to 8.19% – a significant improvement.

Both sensorless speed control and sensorless position control have been implemented using the compensation methods proposed and a $t_{\min}$ of 5 μs. Fig. 13 shows the experimental results of speed reversal at very low speed. The machine is accelerated from standstill to 10 rpm, the speed is then reversed to −10 rpm, and then the motor is brought to standstill. Throughout the test, rated load is applied (i.e. 12.2 Nm). A $6f_e$ periodic fluctuation appears in the speed and the torque current; this is produced by the cogging of the PM machine, and is of a similar level to that measured under fully sensored control. It can be seen that both the steady-state performance and the dynamic response are excellent. The mean speed error is approximately zero, and the peak speed error is approximately 10 rpm at the instant of torque change. The maximum speed error is 3 rpm during steady-state operation. The quality of the sensorless control has not been reduced by the reduction of the minimum vector length.

The proposed sensorless control using FPE also works in the high speed range. Fig. 14 shows the experimental results when the motor is accelerated to 1000 rpm without external load. The dynamic response meets specifications and the estimation errors of both the speed and the electrical position angle are acceptable. The mean speed error is zero. The peak position error is 0.15 rad, with a mean error of 0.06 rad. The latter illustrates the difficulty in obtaining perfect compensation for armature reaction effects, but is considered acceptable.

Fig. 15 shows the experimental results for a sensorless position control test. The machine is driven six rotations from standstill, held stationary for 5 s and then driven six rotations in the opposite direction back to its initial position. In the upper plot, the measured absolute mechanical rotor position angle follows the command position signal very well. At $t = 2.5$ s full load torque is applied, and then released at $t = 4.5$ s. Small disturbances appear on the position waveform at these instants, but the

Table 1 THD of stator currents with different modification schemes

Position estimation scheme	Sensored vector control	INFORM	FPE with standard compensation	FPE with improved compensation
stator current THD, %	4.98	11.56	10.06	8.19

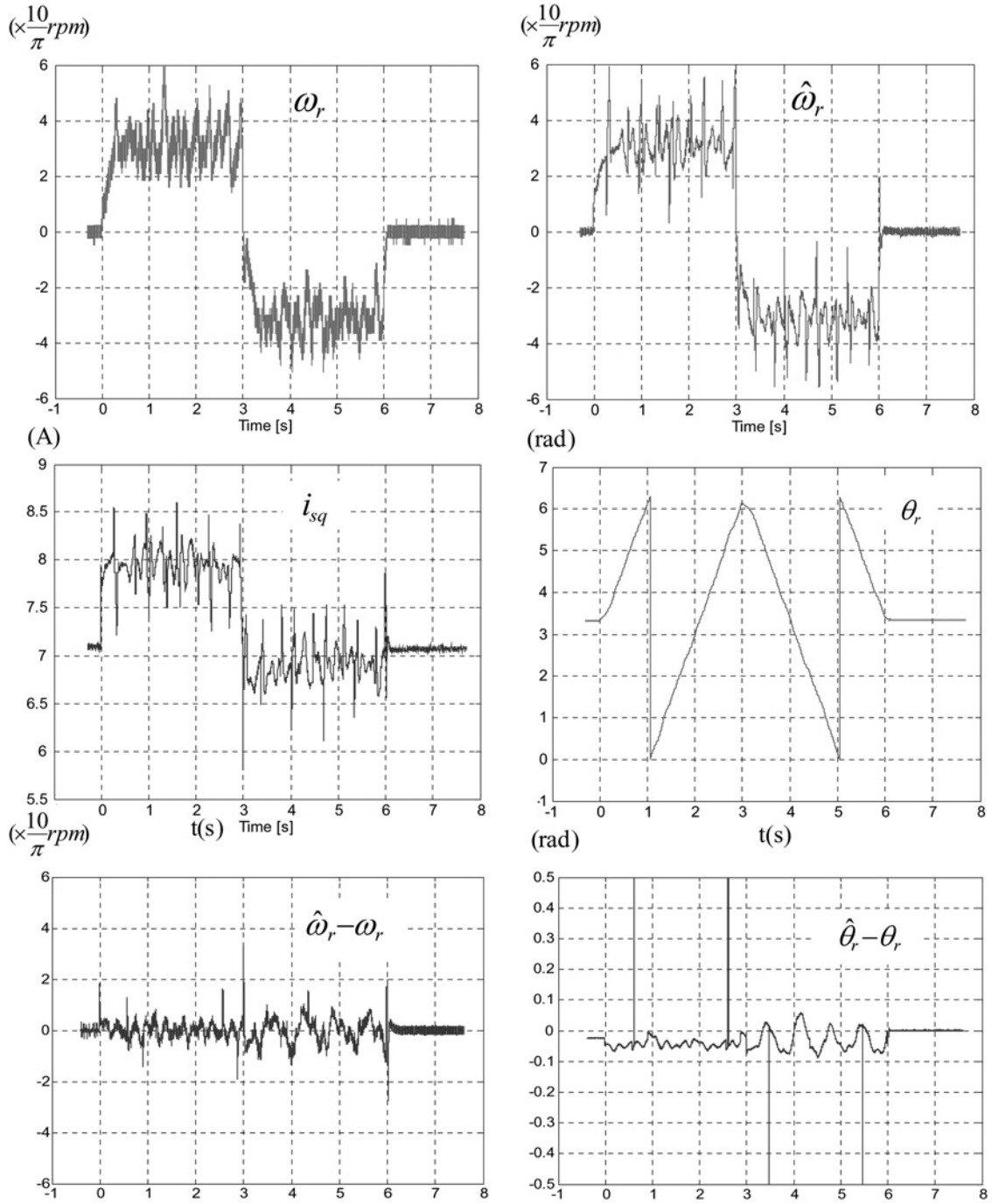

Fig. 13 *Sensorless control results for low speed reversal with full load (0–10–10–0 rpm) ω_r – measured rotor speed, $\hat{\omega}_r$ – estimated rotor speed, i_{sq} – torque current, θ_r – measured rotor angle*

controller is able to quickly recover position with a dynamic response comparable to the fully sensored position control system.

7 Summary

This paper describes the fundamental PWM excitation method for sensorless control, that is, the use of the voltage vectors employed by the normal PWM algorithm in a vector controlled drive to determine the rotor position. The saturation saliency is tracked by measuring the stator current transient response to these voltage vectors.

The accuracy of the current transient (i.e. the current derivative) measurements during narrow voltage vectors is of concern due to the effects of parasitic ringing. If a narrow switching vector exists when di/dt measurements need to be made, these can be extended to improve the di/dt measurement, and the extension can be compensated later in the PWM period using a new compensation technique which employs the opposite switching vector. A new method to analyse the additional distortion caused by the extension/compensation of narrow vectors has also been presented. The analysis demonstrates the effectiveness of the proposed compensation method in reducing the THD of the motor current when narrow switching vectors are present.

The cause of the high frequency parasitic ringing has also been discussed in terms of common mode and differential mode circuits which respond to the high dV/dt imposed on

doi: 10.1049/iet-epa.2010.0108

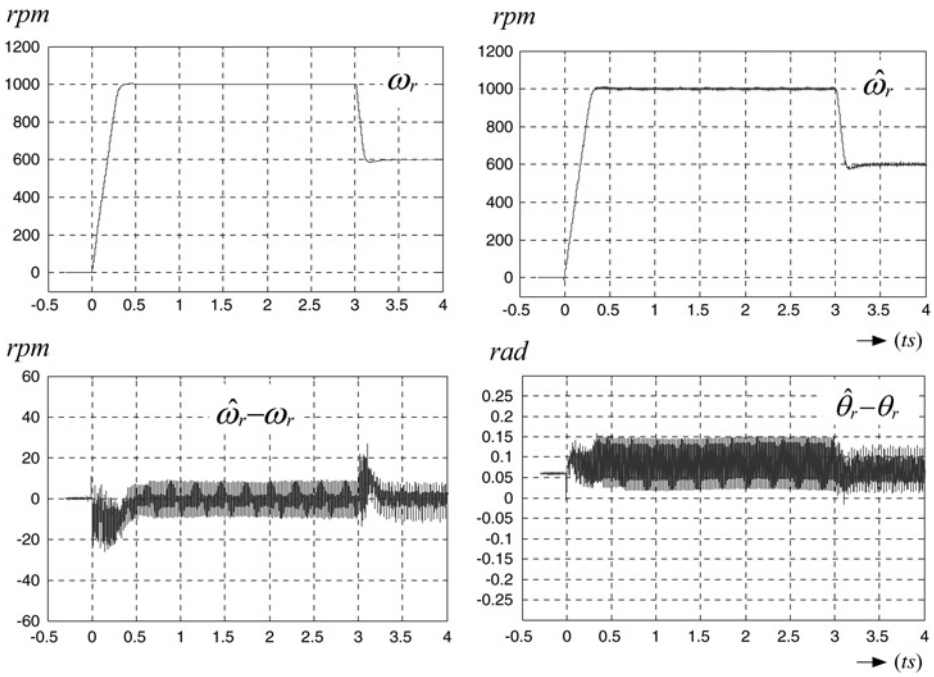

Fig. 14 *Sensorless control results for high speed operation (0–1000 rpm) ω_r – measured rotor speed, $\hat{\omega}_r$ – estimated rotor speed, θ_r – measured rotor angle, ω_r – estimated rotor angle*

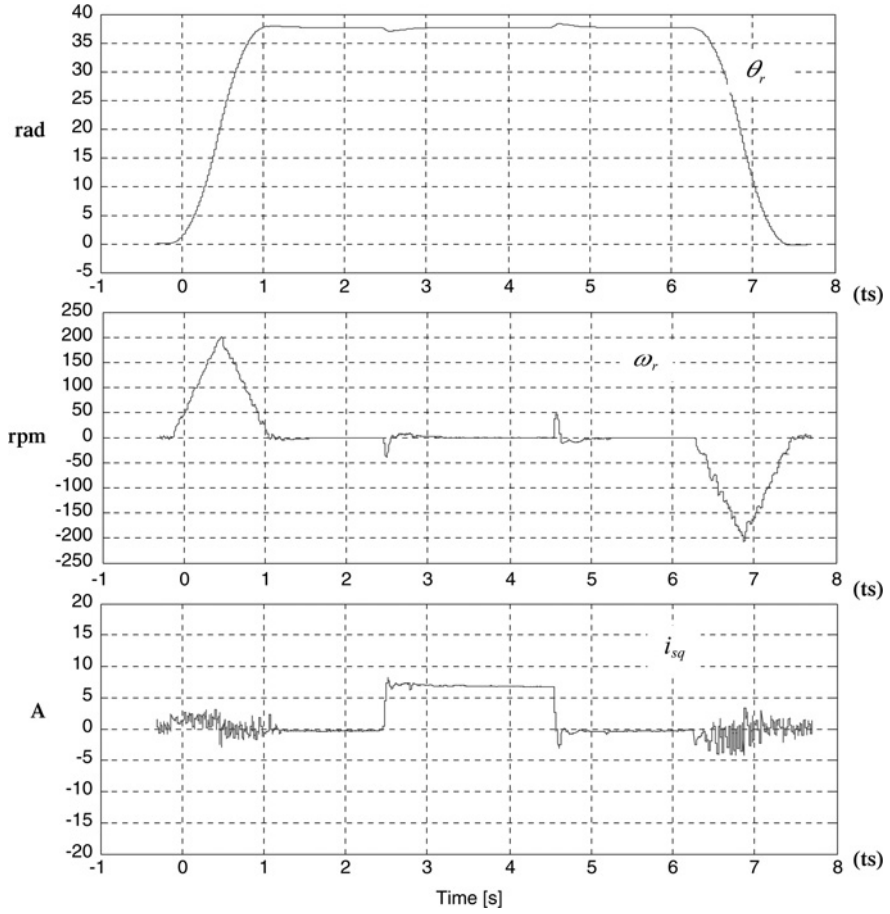

Fig. 15 *Results for sensorless position control: θ_r – measured rotor angle, ω_r – measured rotor speed, i_{sq} – torque current*

the drive when an IGBT changes state. A novel modification to the IGBT gate drive circuit is proposed to increase the gate resistance value and thus to suppress the oscillations during switching periods when di/dt measurement must be made. This effectively decreases the requirement for the minimum vector duration $t_{\min}$. The increase in gate resistance (only

when required for FPE measurement), and the modified compensation method will increase the converter switching losses. The requirement for additional inverter cooling will be dependent on the particular application of the drive. It could be argued that this approach transfers additional motor losses incurred when sensorless control is implemented to the power converter losses and further research is required here. Common mode compensation can also be achieved through a simple software algorithm.

Full sensorless speed and position control have been implemented using the proposed techniques on experimental rig employing a 4 kW surface mounted PMSM. The FPE method with the proposed modifications has been shown to have good steady-state and dynamic performance over a wide speed range.

8 References

1 Jansen, P.L., Lorenz, R.D.: 'Transducerless field orientation concepts employing saturation induced saliencies in induction machines'. IEEE IAS Annual Meeting, 1995, vol. 1, (30), pp. 174–181

2 Holtz, J.: 'Sensorless position control of induction motors – an emerging technology', *IEEE Trans. Ind. Electron.*, 1998, **45**, (6), pp. 840–852

3 Schroedl, M.: 'Sensorless control of AC machine at low speed and standstill based on the INFORM method'. IEEE Industry Applications Society Annual Meeting, Pittsburgh, 1996, 30 September–4 October, pp. 270–277

4 Degner, M.W., Lorenz, R.D.: 'Using multiple saliencies for the estimation of flux, position and velocity in AC machines', *IEEE Trans. Ind. Appl.*, 1998, **34**, pp. 1097–1104

5 Teske, N., Asher, G.M., Sumner, M., Bradley, K.J.: 'Suppression of saturation saliency effects for the sensorless position control of induction motor drives under loaded conditions', *IEEE Trans. Ind. Electron.*, 2000, **47**, (5), pp. 1142–1150

6 Jang, J.H., Ha, J.I., Sul, S.K.: 'Vector control of surface mounted permanent magnet motor without any rotational transducer'. Proc. IEEE Applied Power Electronics Conf. and Exposition (APEC), USA, 4–8 March 2001, pp. 845–849

7 Linke, M., Kennel, R., Holtz, J.: 'Sensorless position control of permanent magnet synchronous machines without limitation at zero speed'. Proc. IEEE Industrial Electronics Society Annual Conf. (IECON), Spain, 5–8 November 2002, pp. 674–679

8 Wolbank, T., Machl, J.: 'A modified PWM scheme in order to obtain spatial information of ac machines without mechanical sensor'. Proc. IEEE APEC, Dallas, TX, 2002, pp. 310–315

9 Holtz, J., Juliet, J.: 'Sensorless acquisition of the rotor position angle for induction motors with arbitrary stator windings', *IEEE Trans. Ind. Appl.*, 2005, **41**, (6), pp. 1675–1682

10 Choi, J., Sul, S.: 'A new compensation strategy reducing voltage/current distortion in PWM VSI systems operating with low output voltages', *IEEE Trans. Ind. Appl.*, 1995, **31**, (5), pp. 1001–1008

11 Holtz, J., Quan, J.: 'Sensorless vector control of induction motors at very low speed using a nonlinear inverter model and parameter identification', *IEEE Trans. Ind. Appl.*, 2002, **38**, (4), pp. 1087–1095

12 Bisheimer, G., Sonnaillon, M., De Angelo, C., Solsona, J., García, G.: 'Full speed range permanent magnet synchronous motor control without mechanical sensorless', *IET Electr. Power Appl.*, 2004, **4**, (35), pp. 35–44

13 Silva, C., Asher, G.M., Sumner, M.: 'Hybrid rotor position observer for wide speed-range sensorless PM motor drives including zero speed', *IEEE Trans. Ind. Electron.*, 2006, **53**, (2), pp. 373–378

14 Hua, Y., Asher, G.M., Sumner, M., Gao, Q.: 'Sensorless control of surface mounted permanent magnet machine using the standard space vector PWM'. IEEE IAS Annual Meeting, USA, 2007, pp. 661–667

15 Gao, Q., Asher, G.M., Sumner, M., Makys, P.: 'Position estimation of AC machines over a wide frequency range based on space vector PWM excitation', *IEEE Trans. Ind. Appl.*, 2007, **43**, (4), pp. 1001–101

16 Ran, L., Gokani, S., Clare, J., Bradley, K.J., Christopoulus, C.: 'Conducted electro-magnetic emissions in induction motor drive system Part I: time domain analysis and identification of dominant modes', *IEEE Trans. Power Electron.*, 1998, **13**, (4), pp. 757–767

17 Narayanan, G., Zhao, D., Harish, K.K., Rajapandian, A., Ranganathan, V.T.: 'Space vector based hybrid PWM techniques for reduced current ripple', *IEEE Trans. Ind. Electron.*, 2008, **55**, (4), pp. 1614–1627

18 SEMIKRON: SEMITRANS IGBT Modules Datasheet SKM 50 GB 123D

19 Holtz, J., Pan, H.: 'Elimination of saturation effects in sensorless position controlled induction motors'. IEEE IAS Annual Meeting, Pittsburgh, USA, 2002, vol. 3, pp. 1695–1702

20 Robeischl, E., Schroedl, M.: 'Optimized INFORM measurement sequence for sensorless PM synchronous motor drives with respect to minimum current distortion', *IEEE Trans. Ind. Appl.*, 2004, **40**, (2), pp. 591–598

doi: 10.1049/iet-epa.2010.0108